Journal of Applied Fluid Mechanics, Vol. 16, No. 9, pp. 1752-1766, 2023.
Available online at www.jafmonline.net, ISSN 1735-3572, EISSN 1735-3645.
https://doi.org/10.47176/jafm.16.09.1755

Numerical Study of Geometrical Properties of Full-Span Tubercle Leading Edge Wing at Post-Stall Condition

A. Nikkhoo and A. Esmaeili†

Mechanical Engineering Department, Faculty of Engineering, Ferdowsi University of Mashhad, Iran

†*Corresponding Author Email: aliesmaeili@ferdowsi.um.ac.ir*

ABSTRACT

In order to upsurge the maneuverability of micro aerial vehicles, a tubercle leading edge inspired by the whale flipper was applied as a passive stall control method. Although this method could be useful to control stall phenomena, the effect of geometrical properties on the flow physic should be investigated to reach the root of them. According to preceding research, the effect of some parameters on the tubercle leading edge wing is a hot topic among researchers. The aim of this research is to explore the effects of sectional wing geometries like amplitude, wavelength, thickness, maximum thickness location, and camber on the aerodynamic feature of full-span tubercle leading edge wing, particularly at 22 degree in post-stall circumstances. The results present that by reducing the amplitude about 2.5%c, the lift coefficient upsurges by about 3.5%; instead, the drag coefficient reduces about 6%. On the other hand, by decreasing the wavelength from 46.2%c to 11.7%c, the drag coefficient and the lift coefficient decrease by about 15% and 19%, respectively. Furthermore, as the thickness rises from 10.55%c to 18.14%c, the lift and drag coefficient goes down about 9.4% and 2.9%, respectively. Furthermore, by increasing the camber from 2.56%c to 3.34%c, the lift to drag ratio goes down by about 1.06%. Finally, by raising the last design variable (maximum thickness location) from 0.26c to 0.51c, the lift to drag ratio increases about 13.7%.

Article History

Received January 14, 2023
Revised March 20, 2023
Accepted April 13, 2023
Available online July 1, 2023

Keywords:

Full-span tubercle leading edge wing
geometrical parameters
Flow Separation Area (FSA)
Air dry zone, aerodynamic forces
Power Spectral Density (PSD)
Fast Fourier Transform (FFT).

1. INTRODUCTION

In the past decade, solutions of some engineering problems have been found through optimization procedures (Nikkhoo & Esmaeili, 2023), inspiration from nature, and a number of new research areas have widely received more attention. Lately, the use of protuberances on the leading edges of wings, fans, hydrofoils, and turbines have been augmented the curiosity of researchers from different areas as an innovative passive flow control technique. The concept was initially influenced by the humpback whale's flipper, which can execute various acrobatic movements including high speed, sharp turns, as well as loops and rolls (Tomilin 1957; Winn, 1985; Mueller & DeLaurier, 2003). The morphology and tubercle leading edge's location exposes the lift increasing to control the flow over the whale's flipper, and also preserving lift at high angles of attack (Brodie, 1977); these lead to delay stall (Fish et al., 2020a).

The alluring abilities mentioned above have captivated the commitment of aerodynamicists to apply similar techniques in actual airfoil and wing designs, particularly on small-scale Micro Aerial Vehicles (MAVs). Since MAVs have small size and normally fly at low velocities then their operating Reynolds number is so low (Re < 200,000). Therefore, the leading edge modification of airfoils and wings like humpback whale flipper has become a hot topic in aerodynamic community in recent years. Numerous investigations have established that applying tubercles could help to diminish the existing issues in the low Reynolds number flow condition. Initially, examinations focused on developing highly particular tapered wings with a high aspect ratio. This was done in an effort to replicate the characteristics of an actual whale flipper, with consideration given to both experimental (Fish et al., 2020b) and computational perspectives (Madsen & Herman 1980). Lately, for different airfoil geometries, Particle Image Velocimetry (PIV) measurements have been carried out (Canning et al., 2011; Delgado et al., 2014; Nili-Ahmadabadi et al., 2019; Liang et al., 2022) to examine the flow behavior around these type of wings.

Nomenclature

A	amplitude	FSA	Flow Separation Area
AOA	angle of attack	FFT	Fast Fourier Transform
c	chord	L	lift force
D	drag force	L/D	lift to drag ratio
CD	drag coefficient	LES	large eddy simulation
CL	lift coefficient	PSD	Power Spectral Density
CP	mean pressure coefficient	RANS	Reynold Average Navier-Stokes
CFD	Computational Fluid Dynamic	Re	Reynolds number
DDES	Delayed Detached Eddy Simulation	SIMPLE	semi-implicit method for pressure linked equations
DES	Detached Eddy Simulation	TLE	Tubercle Leading Edge

Many investigations were conducted subsequently aimed at simulating the tubercle leading edge's effect on idealized whale flippers based on the aforementioned observations. Using both semi- and full-span models such as (Miklosovic et al., 2004, 2007) in wind tunnel tests at Reynolds number ($Re = 3 - 6 * 10^5$) appealed to be within the characteristic operating range for those creatures. In spite of the similar aerodynamics associated with scalloped leading edges in finite and infinite wings, the three-dimensional effects did provide a substantial benefit.

The results illustrate that a large stall phenomenon begins at the the base wing's leading edge, while the leading edge of the wavy wing stalls at the trough region. Due to the sinusoidal wing's high attack angle, the fluid flow attaches to its surface. This allows the lift force to be maintained and even increased after stalling.

To overcome the missed discrepancies in pre-stall condition, some parametric and optimization studies have been done. For example, the experimental study performed by (Hansen et al., 2011) who have compared the performance of NACA 65-021 and NACA0021 airfoils with tubercles at Re = 120,000. It was concluded that the effect of tubercles varies depending on the airfoil outlines and with a profile with its maximum thickness near the chord (NACA 65-021), tubercles have no apparent effect on lift enactment in pre-stall condition and provide an advantage for post-stall. Instead, for the NACA 0021, which has maximum performance in the post-stall area at the expenditure of impaired performance in the pre-stall condition, lift is amplified in the post-stall condition. Furthermore, In studies conducted by (Kelso et al., 2020) and (Chaitanya et al., 2017), it was determined that the optimal stall angle and maximum lift coefficient, as well as the lowest level of drag, were achieved through the utilization of the smallest amplitude and wavelength in tubercle configuration.

In the last few years, experimentally-based parametric investigations have been performed into the influence of tubercles on un-swept finite-span wings demonstrated that tubercles foils generally performed best in terms of lift (Rostamzadeh et al., 2020), drag and efficiency (or lift-to-drag ratio, L/D), with a smaller amplitude and smaller wavelength (Hansen et al., 2010; Custodio et al., 2015). Another investigation was performed by (Bolzon et al., 2016) that was concluded while the wavelength had the least effect, the tubercle phase had the most significant impact on the performance of the wing.

The effects of the roughness element on the wing of the sinusoidal edge with the cross-section of NASA-LS0417 at Reynolds 140,000 had been investigated (Jabbari et al., 2021a), which displayed the effects of functional improvement in relation to the size of laminar separation bubble formation. On the other hand, frequency and acoustic analysis of the effects of roughness on the TLE wing were performed in line with previous research, which presented that by adding the roughness element, the frequency of vortex shedding is observed in this type of wings compared to simple wings (Jabbari et al., 2021b).

The significant effects of tubercle leading edge wings are better aerodynamic performance than baseline wings that they have more lift to drag ratio. To improve these performance of TLE wings, the main aim of this research is to evaluate the effect of 5 design variables that contain amplitude, wavelength, thickness, camber and maximum thickness location at 22 degree in post-stall condition on full-span tubercle leading edge wing and understand the flow phenomena while this changings occurs. to study these changes in the physics of fluid flow, the velocity field and the size of the flow separation around the tubercle wing are compared and their strength and size were examined by performing frequency analysis of vortices. This investigation will greatly help future research to select the best dimensions for these five design variables in order to achieve the best aerodynamic features and circumstance.

This paper is structured as follows. The numerical tools, problem formulation and baseline geometry used in this work are designated in Section 2. The CFD mesh, Y plus and validation are introduced in Section 3. Finally, the results of geometrical parameters effects simulations and contours and graphs are compared and examined in section 4.

2. NUMERICAL SIMULATION

In order to model the wavy leading edge infinite wing, and also to create protuberances on the wing at the leading edge, the mathematical equation according to related studies (Esmaeili et al., 2018; Esmaeili & Nikkhoo, 2021), the leading edge of the tubercle wing was designed to resemble the tubercle cross-section of the Humpback whale.

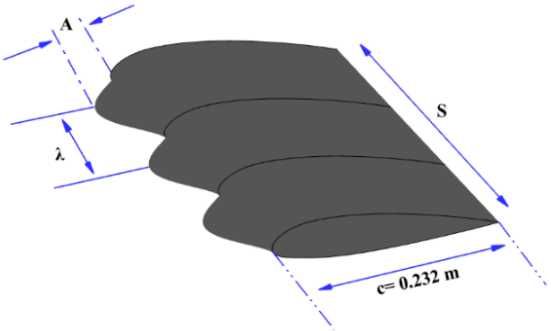

(a) Tubercle leading edge wing

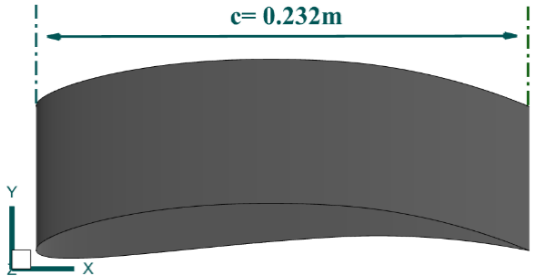

(b) Baseline wing

Fig. 1. Wing geometry.

In the above equation, A represents the amplitude and λ represents the protuberances' wavelength, respectively. The tubercle leading edge and baseline wing that are used in this study are shown in Fig. 1, where A represents the amplitude and λ represents the wavelength of the wing. It is worth mentioning that the chord length of this airfoil is 232 mm.

In this study, Ansys Fluent 19, a commercially available software, is employed as the solver. Throughout the simulation, a time-independent solution procedure is utilized and the no-slip condition is set for the desired geometry. Based on the mean chord length, the Reynolds number is 1.4×10^5. The Turbulent intensity in this study is mild and is set at about 1%.

As stipulated by the physics involved in the current investigation, while conducting numerical simulations, it is necessary to solve the Navier-Stokes equations by the finite volume method (Esmaeili et al., 2018). The Detached Eddy simulation (DES) turbulence model has been used. This perturbation model is actually a combination of the k-w SST and LES models, which uses the RANS model in areas close to the wall and the large eddy Simulation (LES) model in areas far from the wall where the eddies are larger. However, the connection between the LES and RANS areas operates routinely, and no user definition is required. It is noteworthy that in recent years, in order to address some of the weaknesses of the model, modifications have been made to provide models of Detached Delayed Eddy Simulation (DDES) and Improved Detached Delayed Eddy Simulation (IDDES). In this study, the conservative F2 shielding in DES to better approximate the experimental data is used due to the proper capture of the flow separation area (FSA) above the upper surface of the wing.

The numerical method employed a SIMPLE (which

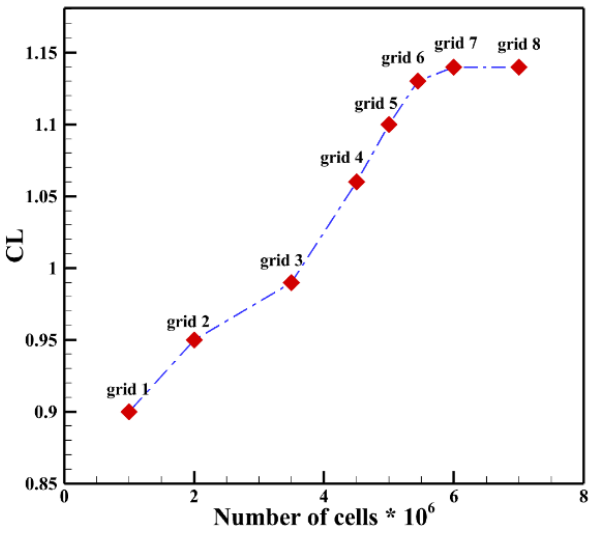

Fig. 2. Mesh independency of tubercle leading edge wing at 22 degree in post stall condition.

outlooks for the semi-implicit method for pressure linked equations) pressure–velocity coupling and a second-order-accurate spatial discretization for the pressure.

Furthermore, the quadratic interpolation formula of the QUICK (which stands for quadratic upwind interpolation for convective kinematics) scheme (Pereira & Sousa, 1993) was used in the finite volume discretization of the transport equations. However, the process of time integration is carried out using a second-order precise implicit approach to mitigate constraints on numerical stability. Simulations reported herein used a time step of 0.0025 s, with a preliminary reduction of halving this value to confirm time-step independence. In the preliminary stage, the time value was half divided to substantiate the autonomy of the time step. The results revealed the satisfactory accuracy of the investigated time value, hence, validating the temporal independence of the outcomes. When setting the numerical simulation parameters, the values of the wing chord are 232 mm and the Reynolds number is 140,000, which in this case corresponds to the free flow rate $U_\infty = 8.814$ of m/s.

3. COMPUTATIONAL DOMAIN, MESH STUDY AND NUMERICAL VALIDATION

The mutual C-H topology is used to generate grids as the computational mesh in the infinite tubercle wing's numerical simulation. Mesh independency is also done by altering the number of meshes as it reveals in Fig. 2. Thus, the simulation has 6 million mesh grids. In addition, the concluding mesh type around the model is revealed in Fig. 3.

In order to examine the boundary condition and domain of the simulation, Fig .4 reveals the wing position and other information. The selection of the fundamental domain with the highest utility has been made in order to create a rational correlation between the quality of the solution and the computation. The condition of outlet pressure boundary is employed at the boundary of the output, placed 12c away from the wing's trailing edge.

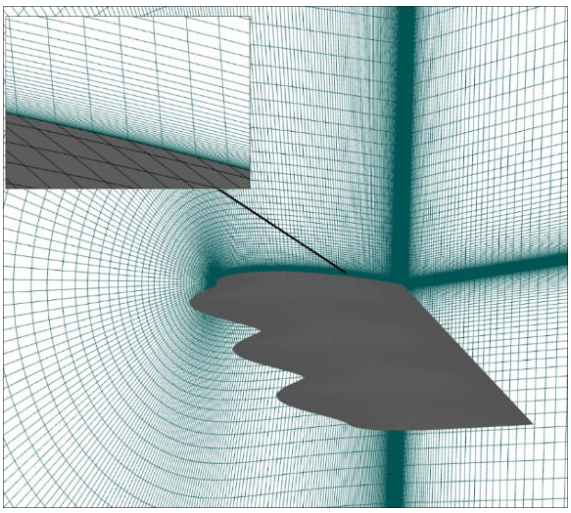

Fig. 3. Computational mesh around the model at 22 degree in post stall condition

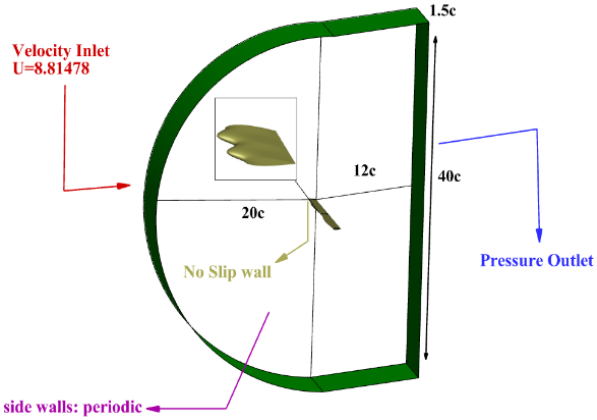

Fig. 4. Boundary condition of current simulation.

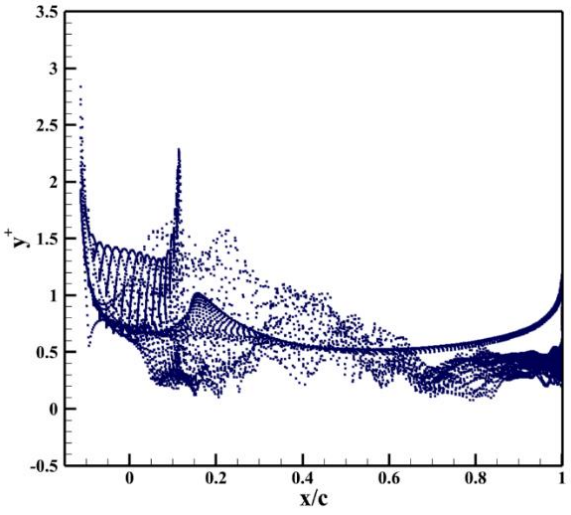

Fig. 5. Y plus of tubercle leading edge wing at 22 degree in post stall condition.

Additionally, all surfaces of solid walls are subject to no-slip conditions, which can be clearly comprehended in Fig. 4. According to Menter (Langtry et al., 2006), in order to properly capture the transitional and laminar boundary layer, it is necessary to adjust the value of y^+ to about one and it reveals in Fig. 5. More over, in the present work, According to the flow turbulence model, the value varies in an appropriate range.

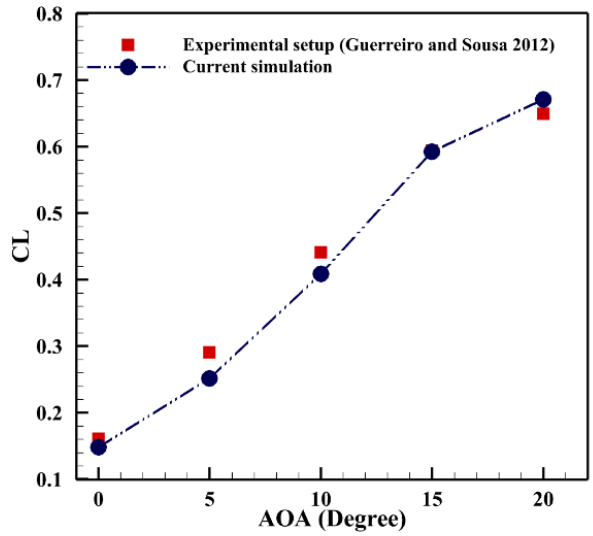

Fig. 6. Comparison between lift coefficient of the numerical and experimental tubercle leading edge wing with AR=1.

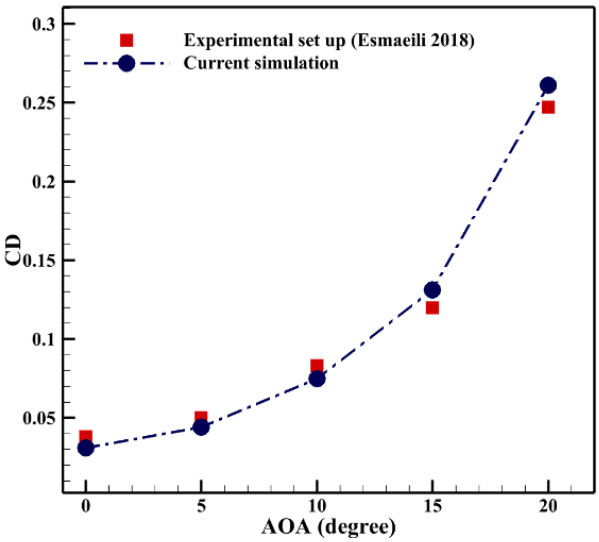

Fig. 7. Comparison between drag coefficient of numerical and experimental of tubercle leading edge wing with AR=1

To verify the numerical methodology, it is essential to compare the current numerical solution results with the experimental data (Guerreiro & Sousa, 2012; Esmaeili, 2018). The numerical solution and experimental values of lift coefficient and drag coefficients of tubercle leading edge wing are exposed in Fig. 6 and Fig. 7. The numerical results of the simulation of wing's aerodynamic coefficient are in very good agreement with the experimental results, especially at the higher angle of attack. The beginning of the drag coefficient of the wing is at zero degree and increases with the increase of the angle of attack until the separation time. The faster increase in drag after the angle of attack of 10 degrees

indicates the flow separation caused by the adverse pressure gradient in the boundary layer.

All experiments with the validation's references were performed at the low-speed open-circuit wind tunnel. The rectangular cross-section with an area of 1.35 × 0.8 m^2, was considered for the wind tunnel's test section. In addition, the free stream velocity was set to 10 m/s and the turbulence intensity was 0.3% in the potential core of the open jet. Data set information, freestream velocity, and AOA were accomplished via AeroIS. For measuring the aerodynamic forces, a custom-made six-component Schenck compact balance was employed a single-strut model provision connected to the load cells. The study utilized the methodology proposed by (Coleman & Steele, 2012) to assess bias uncertainties impacting force coefficients at a 95% confidence level, resulting in maximum uncertainties of 5% for lift and drag. However, in the case of the latter coefficient at low incidences and aspect ratios, these uncertainties may be twice as significant, as indicated by (Guerreiro & Sousa, 2012). The experimental data were adjusted for wind tunnel corrections, which accounted for load component interactions, open jet operation, and weight tares (Barlow et al., 1999). Furthermore, a specialized investigation was conducted to address model-mount interactions and provide supplementary corrections to the experimental data.

4. RESULTS AND DISCUSSION

In this study, the geometrical parameters of the infinite tubercle wing are considered and the physics of fluid flow around the infinite tubercle leading edge wing is investigated at 22 degree attack angles in post-stall condition and a critical Reynolds number (1.4×10^5). As mentioned before, not much attention has been paid to geometrical parameters in the post-stall circumstance, to better understand the performance of the flow distribution around the tubercle leading edge wings during variation of amplitude, wavelength, thickness, camber and maximum thickness location and the effects of these five parameters. This examination helps to better understand the best measurements of these design variables to select and performed at post stall conditions. The procedure of the examination is about each one of these design variables simulating while others are considered as constant.

4.1 Amplitude Effect

The first geometry parameter which can inspire flow physics is the sectional amplitude of the sinusoidal leading-edge wing at post stall region. Thus, this section divulges the majority of flow behavior around the wing when amplitude has changed when other design variables are constant. Initially, to assess aerodynamic performance of infinite wing, lift and drag coefficients are compared in Table 1 for three variations of amplitude ratios.

It can be seen that as the sectional amplitude in the infinite tubercle wing goes down from 8.3%c to 5.8%c, the lift coefficient increases and in fact, the drag coefficient diminishes. As a matter of the fact, the aerodynamic coefficients are strongly influenced by the

Table 1 Majority of three different amplitude at attack angle of 22 degree

Case No	amplitude	CL	CD	(L/D)
I	8.3%c	0.84	0.35	2.40
II	7.8%c	0.86	0.35	2.45
III	5.8%c	0.87	0.33	2.61

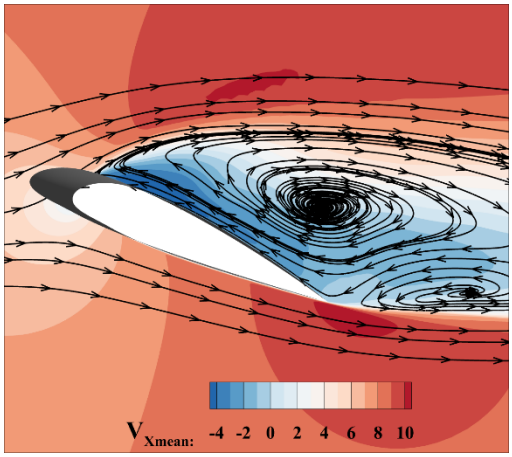

(a) Case II (amplitude ratio 7.8%c)

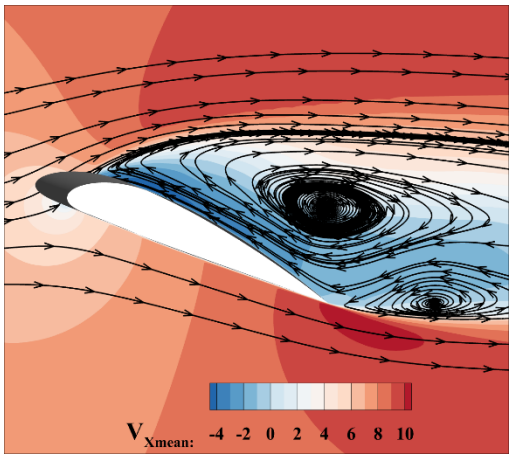

(b) Case III (amplitude ratio 5.8%c)

Fig. 8. Mean x-velocity contour and flow streamlines between two different amplitude.

size of the flow separation area (FSA). It would be obvious from the below table that by reducing the amplitude ratio the lift to drag ratio goes up.

The most outstanding consequence of capricious mean streamwise velocity (x-velocity) dissemination is exposed in Fig. 8 for two tubercle wings with different sectional amplitude ratios. According to Fig. 8, while the amplitude reduces from 7.8%c to 5.8%c, the flow separation's size and strength detected at the former spanwise location have been significantly abridged for the altered geometry. Thus, the results show more reduces amplitude is, the more decrease FSA size. Hence, this leads to drag coefficient reduction.

Furthermore, the accelerated flow area in the suction side of the infinite wing becomes larger in case II; since the flow in the upper layers of the suction side of the wing

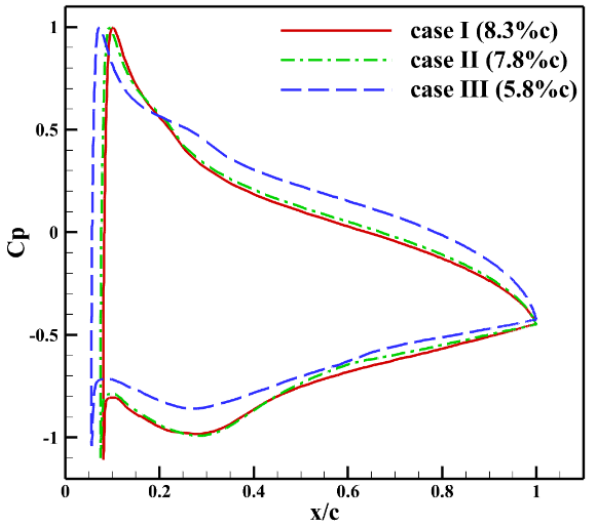

Fig. 9. Mean pressure coefficient of three different amplitude ratio Comparison between.

is more energetic, the turbulent mixing process redeploys high momentum fluid inside the lower layer of flow near the surface and the flow is squeezed, which is resulted from a gain in lifting force. In addition, the retraction of the amplitude caused the center of the vortices to move away from the wing surface. Because of that, the amount of momentum transfer of the flow to the area behind the vortex has increased in case III; this has led to lift growth.

The mean pressure coefficient distribution along spanwise between three different amplitude ratios is revealed in Fig. 9. When the separation bubble is about to

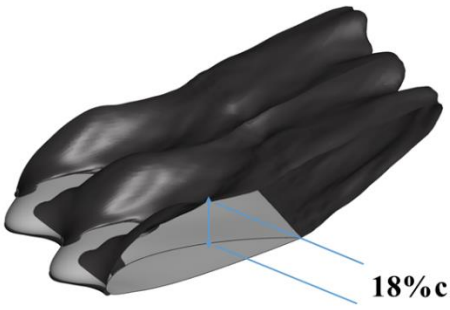

(a) Case II (amplitude ratio 7.8%c)

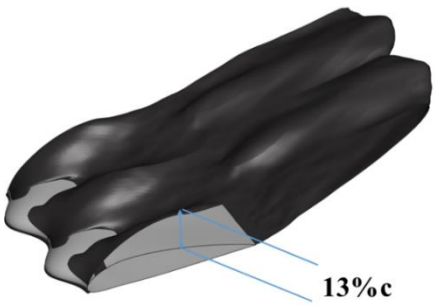

(b) Case III (amplitude ratio 5.8%c)

Fig. 10. Iso surface of zero streamwise velocity for two variations of the sectional amplitude ratio.

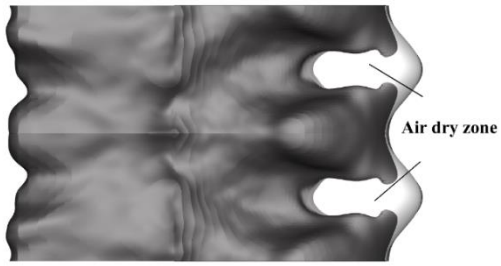

(a) Case II (amplitude ratio 7.8%c)

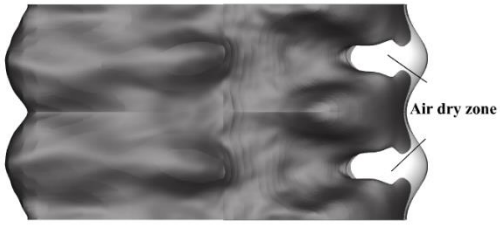

(b) Case III (amplitude ratio 5.8%c)

Fig. 11. Air dry zone measurements of two different amplitude cases.

form, the pressure inside the bubble will be constant; For this reason, in the figure above, the areas from the upper surface of the wing where the pressure coefficient is almost fixed to the line indicate the location of the bubble.

By comparing these three diagrams, it can be seen that the length of the bubble in case I is about the same exact amount to case II and also it's greater than in case III, because the pressure, in this case, remains constant up to a longer length than the wing surface. Finally, a higher pressure difference is obvious in case III and from the basic of aerodynamics; the more pressure difference is, the more lift coefficient would be apparent and that would clearly show that case III has more lift than others.

A clear picture of flow separation area width and height is revealed in Fig. 10 by plotting iso-surfaces of zero time-averaged streamwise velocity. The effect of the sectional amplitude ratio on the FSA height can be mentioned in this figure. As a matter of the fact, it has been demonstrated that the FSA's height is 18% of the mean chord in a higher sectional amplitude ratio (7.8%c) and it has been lessened to 13% of the mean chord in case III (5.8%c). Moreover, the FSA's width became smaller by reducing the sectional amplitude ratio.

The air dry zone is the region that contains a non-laminar separation bubble (LSB) or non-flow separation area (FSA) in that area and when any iso surface extracts the non-flow area is air dry zone. Subsequently, by measuring these two cases in Fig. 11, this study reveals that case II has 0.0126 m^2 Air dry zone and case III has 0.0190 m^2 air dry zone. Thus by decreasing the amplitude from 7.8%c to 5.8%c, the air dry zone rises up to by about 0.0064m^2. As a matter of the fact, this would conclude from the results that the air dry zone has reverse relation with drag coefficient. In addition, by the more reduction in amplitude, the more air dry zone would occur and this leads to the drag coefficient reduction too.

Table 2 Majority of two different wavelengths at an attack angle of 22 degree

Case No	wavelength	CL	CD	(L/D)
IV	46.2%c	0.84	0.35	2.40
V	11.7%c	0.71	0.30	2.36

Table 3 Majority of three different thicknesses at an attack angle of 22 degree

Case No	thickness	CL	CD	(L/D)
VI	10.55%c	0.85	0.34	2.50
VII	13.63%c	0.79	0.34	2.32
VIII	18.14%c	0.77	0.33	2.33

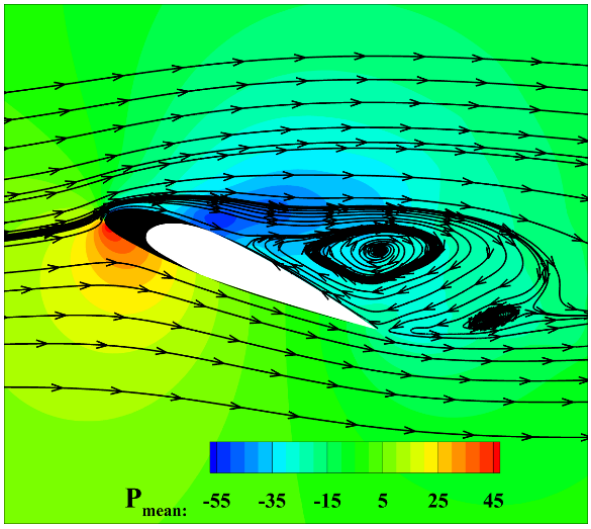

(a) Case IV (46.2%c)

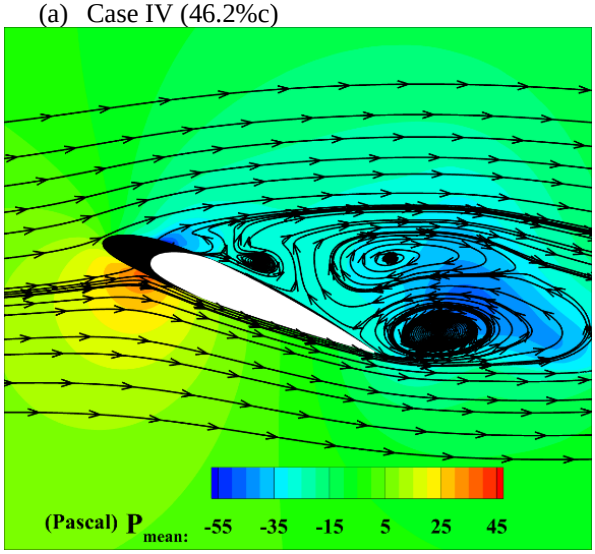

(b) Case V (11.7%c)

Fig. 12. Mean pressure contour and flow streamlines between two different wavelength.

4.2 Wavelength Effects

Thus, the second design variable that this study wants to evaluate, is considered as the wavelength to reveal the flow behavior during its changes. Table 2 presented the majority of wavelength variety of two different cases. The results demonstrate that by reducing the wavelength from 46.2%c to 11.7%c the lift and drag coefficient goes down. Even though the lift to drag ratio (L/D) has the exact direct relation with wavelength reduction and it goes down too.

For more details, this study reveals the mean pressure contour in the trough section of the wing and the flow streamline in the mid-plane and wing surface in Fig. 12. The results determine that the airfoil wavelength ratio could play a significant character on the size of separation and consequently changes the flow decoration and aerodynamic features. As shown in Fig. 6, the separation procedures in both cases but the difference is that; the size of separation in case IV is bigger than case V, so this means, by reducing the sectional wavelength ratio from 46.2%c to 11.7%c, the length of separation area gradually declines and the flow reattachs to the end of the wing's trailing edge. This incident leads the mind to the fact that by decreasing the separation size the drag coefficient goes down, thus by comparison to table 3, the results prove that the drag coefficient reduces by reduction of wavelength. As seen in the overhead figure; in case IV on the wing surface, the case has lack pressure because of the contour color, and also it is obvious from the lower wing that case IV has higher pressure in the leading edge and this leads to the opposite side of the mind thinking that contain more velocity and concludes that case IV has more lift coefficient. In order to better juxtaposition these two cases, the streamlines extracted from the contour in the above figure. For this purpose in case IV (46.2%c) the flow separates from leading edge and re-attach to the surface at the trailing edge, it can be seen the big vortex in the middle of the chord of this wing that causes a larger separation size and again the second vortex formed after trailing edge. Even though in the case V (11.7%c) small vortex is established at leading edge and the flow reattaches at the middle of the chord and the second and third vortex establishes too. Hence, the distance of the vortex that formed after trailing edge is fascinating. The third vortex in case V is much closer than the second vortex in case IV, thus this could be the proof of the flow velocity power and the higher lift that case IV has.

Hence, to share the information of the velocity distribution around two tubercle leading edge wings with different wavelengths, this investigation goes through the Mean x velocity and illustrates it in Fig. 13. From the previous sections the flow separation area (FSA) size of case IV (46.2%c) is much higher than case V (11.7%C). Actually, the separation thickness (height) causes to change the flow acceleration in the upper layers and momentum removal from the upper layers to inside the separation has altered. As shown in Fig. 13, the height of separation in a higher wavelength ratio (case IV) is bigger than that of in case V and consequently, the drag coefficient in this case (wavelength ratio of 7%c) has been increased.

Also, from the upper surface of these two cases, the momentum and flow acceleration in the red section of the contour reveals that case IV has much higher acceleration and this proves more lift coefficient this case has.

In conflict with the former clarification, the wavelength can change the flow separation size (its length). This is demonstrated here in Fig. 14, illuminating

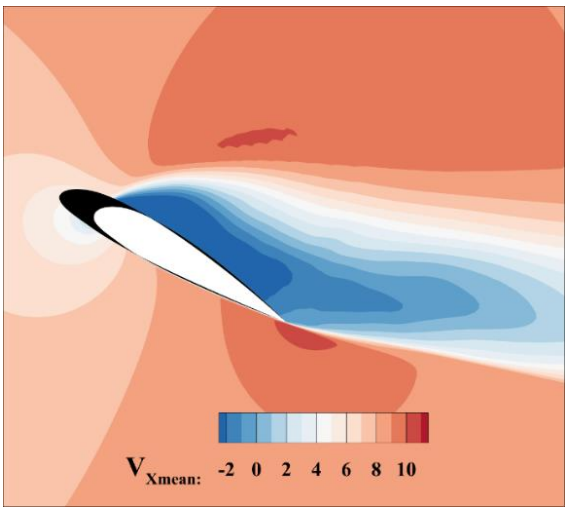

(a) Case IV (46.2%c)

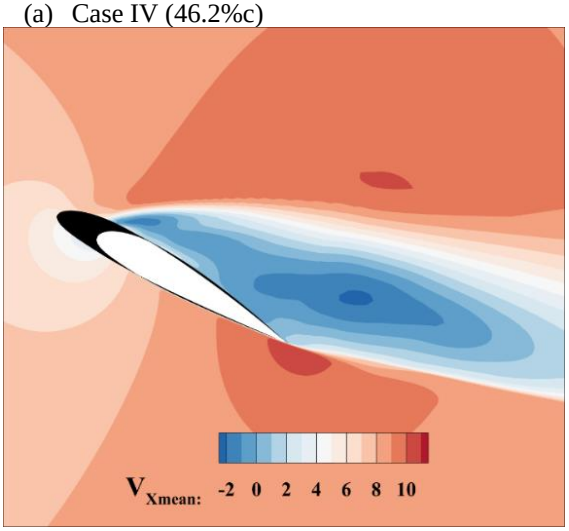

(b) Case V (11.7%c)

Fig. 13. Mean X velocity between two different wavelengths.

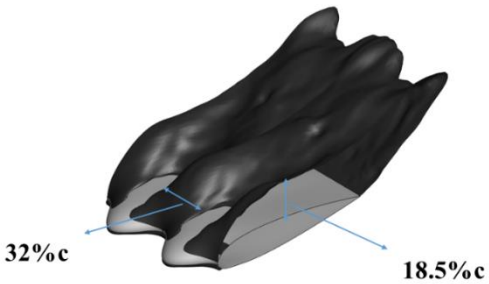

(a) Case IV (46.2%c)

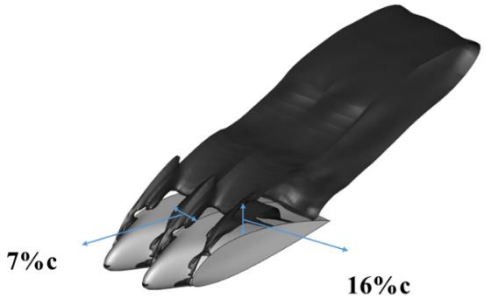

(b) Case V (11.7%c)

Fig. 14. Iso surface of zero streamwise velocity for two variations of sectional wavelength ratio.

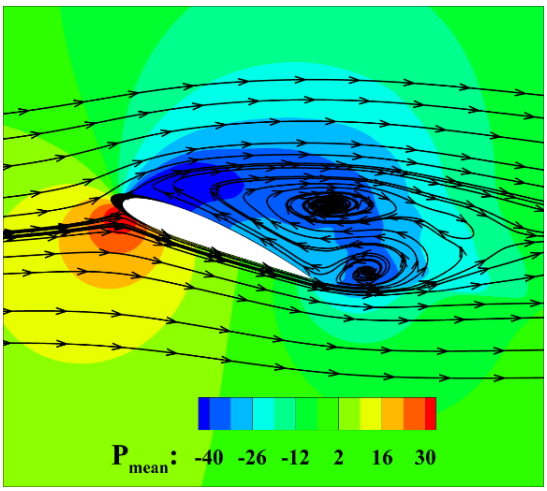

(a) Case VII (thickness ratio 13.63%c)

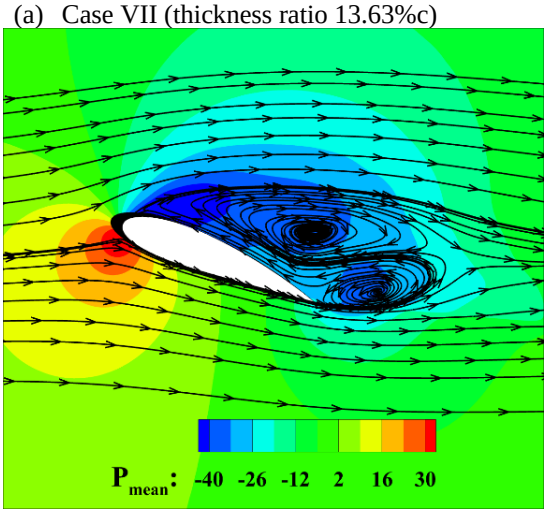

(b) Case VIII (thickness ratio 18.14%c)

Fig. 15. Mean pressure contour and flow streamlines between two different thickness ratios.

the three-dimensional iso surface x velocity. By the results revealed in the above figure, this study concludes that by reducing the wavelength from 46.2%c to 11.7%c, the height of the laminar separation bubble is going down and decrease by about 2.5%Chord and also the width of the flow separation area reduces about 25%c. So case IV has much drag coefficient than case V.

4.3 Thickness Effects

Another geometrical parameter for exploratory the best value of parameters that influenced the aerodynamic performance of the aforementioned wing is airfoil sectional thickness. Hence, this section demonstrates the majority of flow distribution around the sinusoidal wing while the sectional thickness ratio has rehabilitated. In order to assess the aerodynamic performance of infinite wings, the juxtaposition of lift and drag coefficients between two tubercle leading edge wings with various thickness ratios has occurred in Table 3. Thus, it can be concluded that by increasing the thickness ratio from 10.55%c to 18.14%c lift coefficient and drag coefficient act reversely and go down. To see the reason for these results, this study examines a lot of modules to examine the reasons.

The mean pressure contour in the trough section of the wing and the flow streamline is illustrated in Fig. 15. As it

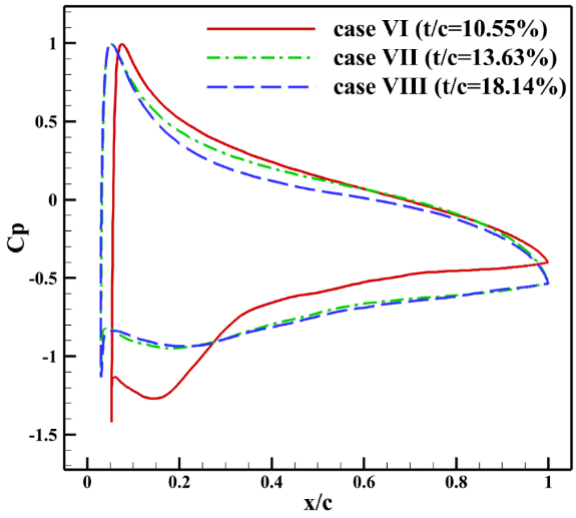

Fig. 16. Mean pressure coefficient of three different thickness ratios.

obvious, the separation of flow occurs at the leading edge and then reattaches to the wing surface at the middle of the chord, and flow separation area performs at the upper surface of wing. As presented in Fig. 15, the FSA forms in both cases but the difference is that the FSA in case VII is bigger than case VIII, so this means, by growing the sectional thickness ratio from 13.63%c to 18.14%c, the length of FSA gradually decreases. Meanwhile, the bubble height in case V (t/c=13.63%) is higher compared to case VIII (t/c=13.63%), the boundary layer behind the FSA has fully-fledged and a secondary separation has ensued near the trailing edge, which can be part of drag coefficient progress in inferior thickness ratio.

As exposed in Fig. 16 the mean pressure coefficient distribution along spanwise between three different amplitude ratios is examined. by comparing these three diagrams, it can be seen that the length of the bubble in case VI is about the same amount in case VII and also it's greater than in case VIII, because the pressure, in this case, remains constant up to a longer length than the wing surface. Furthermore, case VI has a large amount of pressure difference and it obviously has more lift coefficient other than the two other cases. Eventually, case VII has a little bit more pressure difference than case VIII, this leads to the fact that case VII has more lift coefficient than case VIII.

The effect of the sectional thickness ratio on the FSA width can be mentioned in Fig. 17. More ever, it has been validated that the FSA height is 26% of the mean chord in the lower sectional thickness ratio (10.55%c) in case VI and it has been decreased to 17.5% of the mean chord in case VIII (18.14%c). Moreover, the FSA width became thinner too, by increasing the sectional thickness ratio from 26%c to 24%c. Therefore, the flow can disseminate in spanwise direction when the thickness ratio is grown and FSA height will be declined, assigning to the drag coefficient bargain.

According to the previous accomplish, the Air dry zone is part of the area that has no iso surface non-velocity streamwise (u=0) in that zone. This fact demonstrates in Fig. 18, and also the above figure tries to show the reader:

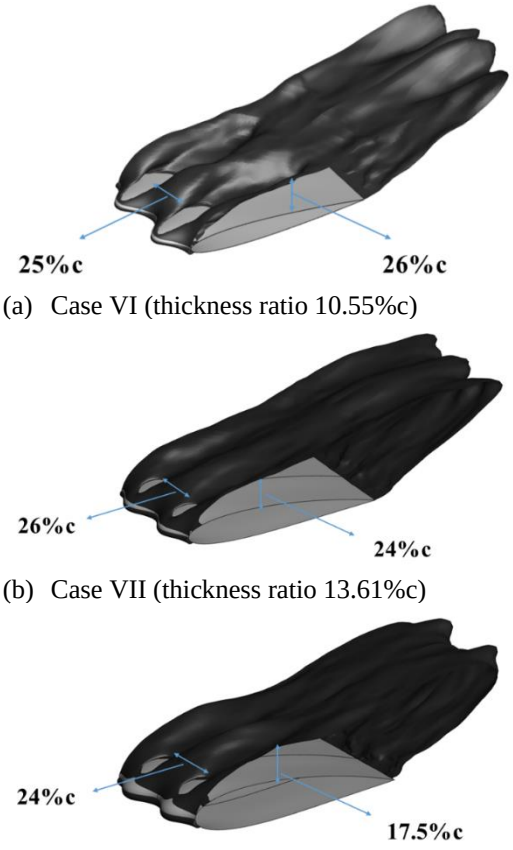

(a) Case VI (thickness ratio 10.55%c)

(b) Case VII (thickness ratio 13.61%c)

(c) Case VIII (thickness ratio 18.14%c)

Fig. 17. Iso surface of zero streamwise velocity for three variations of sectional thickness ratios.

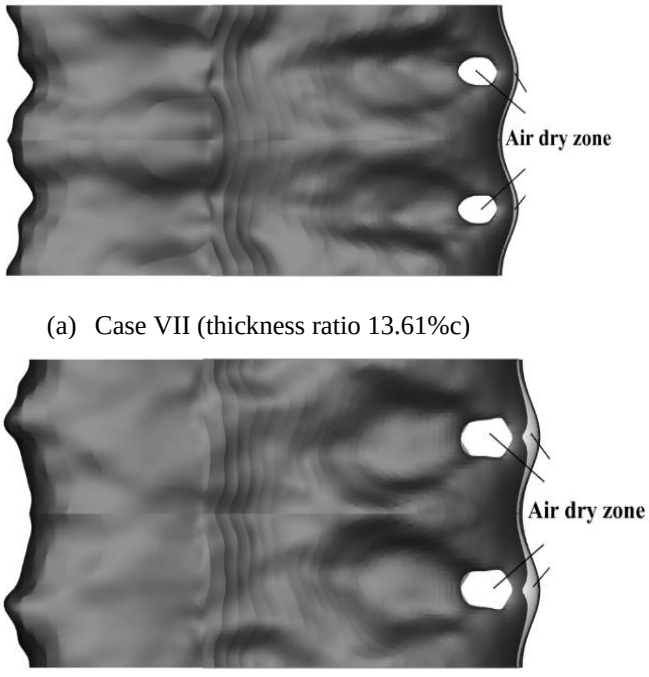

(a) Case VII (thickness ratio 13.61%c)

(b) Case VIII (thickness ratio 18.14%c)

Fig. 18. Air dry zone measurements of two different sectional thickness ratios.

what would occur to Air dry zone while the thickness ratio changes. As seen in Fig. 18; case VII has 0.005 m^2 and case VIII has 0.0014 m^2. Thus according to that, by

Table 4 Majority of three different camber at an attack angle of 22 degree.

Case No	camber	CL	CD	(L/D)
IX	2.56%c	0.84	0.35	2.40
X	3.34%c	0.86	0.36	2.38

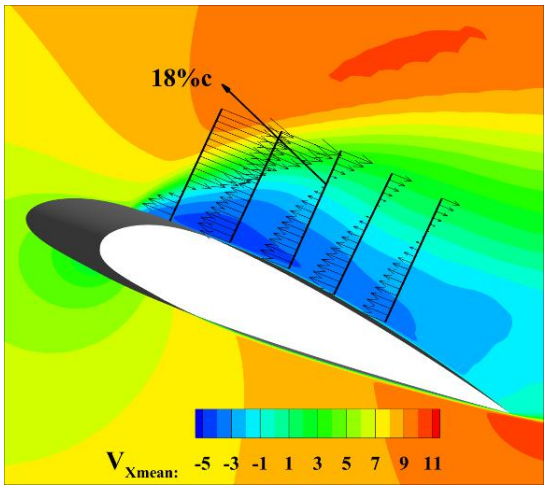

(a) Case IX (2.56%c)

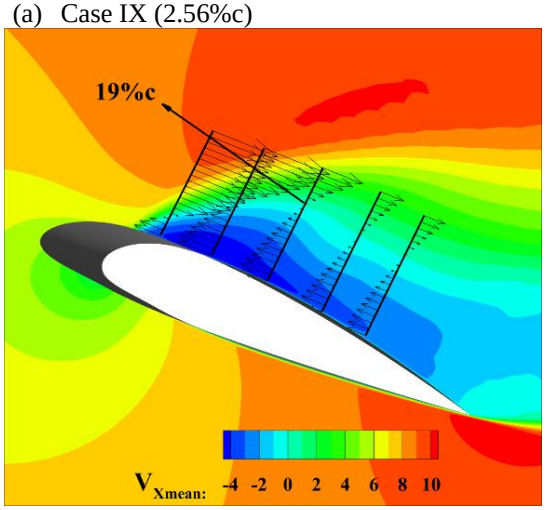

(b) Case X (3.34%c)

Fig. 19. Time-averaged streamwise velocity for two different sectional camber.

increasing the thickness ratio from 13.63%c to 18.14%c the Air dry zone growth about 0.0036 m^2 and by the fact that Air dry zone and drag coefficient's inverse relation; the drag coefficient goes down, too.

4.4 Camber Effects

In order to previous functions, the fourth geometrical parameter that affects the aerodynamic procedure of the aforesaid wing is sectional airfoil camber. So this part evaluates the flow distribution around the sinusoidal wing when the sectional camber has changed. The juxtaposition of drag and lift coefficients among two sinusoidal leading-edge wings with various camber has occurred in Table 4. As seen below table changing camber has the exact direction between the drag coefficient and lift coefficient; this could be the result that by reducing the camber these two aerodynamic forces decrease too. Moreover, by increasing the camber ratio, the lift to drag ratio goes down.

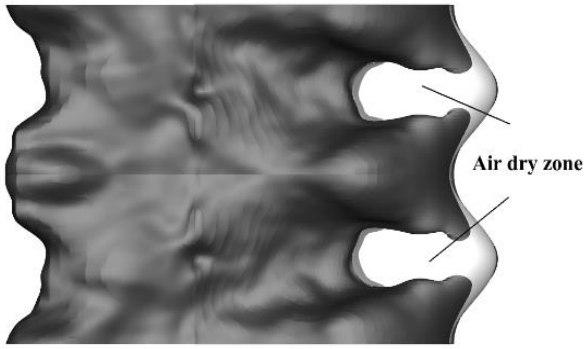

(a) Case IX (2.56%c)

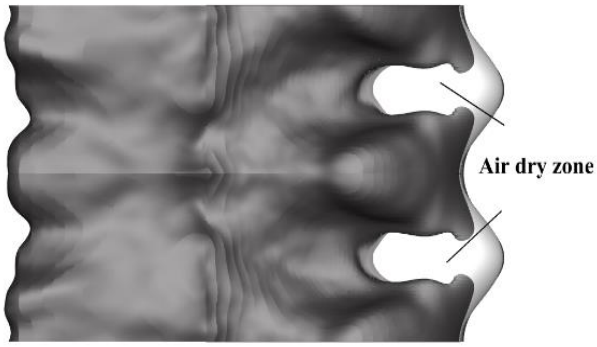

(b) Case X (3.34%c)

Fig. 20. Air dry zone measurements of two different sectional camber.

Based on information exchange and problem analysis of the variation of different camber effects, Fig .19 compares the flow separation area height of the two wavy leading edge wings. The bubble height in case IX is 18%c while this height in case X is about 19%c. As a matter of fact, this study concludes that by growing the camber from 2.56%c to 3.34%c, the height of the flow separation area increases around 1% of the mean chord, and this leads to drag coefficient rising.

In order to examine the Air dry zone discussed in the aforementioned sections before, Fig. 20 has a clear picture of two iso surfaces of the streamwise velocity of tubercle leading edge wings. Thus, this section compares these two cases while the sectional camber changed. According to the above Figure by increasing the camber from 2.56%c to 3.34%c, the Air dry zone increase about 0.0248m^2. This means that Air dry zone has an inverse relation with FSA.

4.5 Maximum Thickness Location Effects

Another geometrical parameter which can influence flow physics is the sectional maximum thickness location of the infinite tubercle leading edge wing. Thus, this section reveals the majority of flow behavior around the wing when the maximum thickness location has changed when other design variables were constant. Initially, to gauge the aerodynamic features of the infinite wing, lift and drag coefficients are compared in Table 5 for various maximum thickness location ratios. It can be seen that as the sectional maximum thickness location in the infinite

Table 5 Majority of three different maximum thickness locations at an attack angle of 22 degree

Case No	Max thick location	CL	CD	(L/D)
XI	0.26 c	0.87	0.33	2.63
XII	0.48 c	0.97	0.35	2.77
XIII	0.51 c	1.1	0.36	3.05

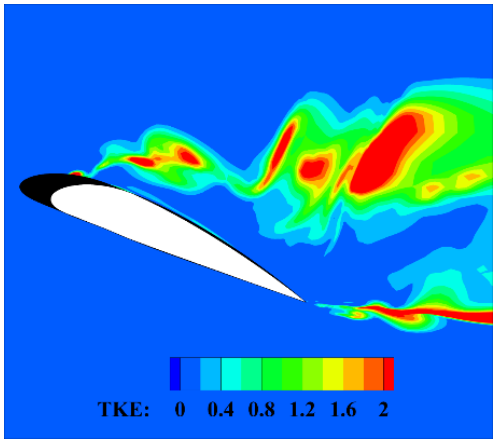

(a) Case XI (0.26 c)

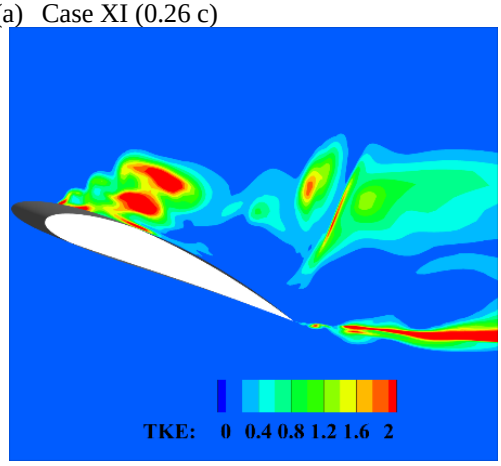

(b) Case XII (0.48 c)

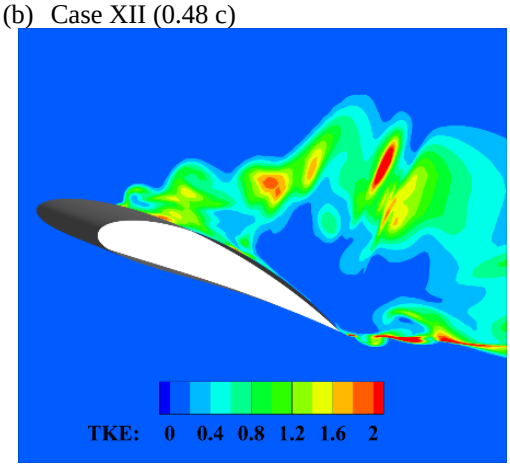

(c) Case XIII (0.51 c)

Fig. 21. Turbulent kinetic energy of three different maximum thickness location ratios.

tubercle wing grows from 0.26 c to 0.51 c, the drag coefficient and lift coefficient increases. In turn, increasing the lift to drag ratio (L/D) would be visible. As declared in the prior division, the aerodynamic coefficients are strongly influenced by the size of the flow separation area.

In addition, the analysis of turbulence kinetic energy around the infinite tubercle leading edge wing for different camber ratios can help in a better understanding of the flow mechanism and it reveals in Fig. 21. Turbulence kinetic energy is the average kinetic energy per unit mass applied to eddy in a turbulent flow. Therefore, based on the mentioned contour, it can be seen that in case XII, the area with high turbulence intensity is close to the wing surface, and a larger part of the wing chord is covered by this area. This causes the separated bubble flow to return to the surface faster and at a shorter distance, and in this case, more momentum is transferred.

On the other hand, the upsurge in the turbulent kinetic energy is affected by the intensification in the velocity gradient on the surface of the airfoil, and as a matter of the fact, by growing the kinetic energy of the particles, the bubble phenomenon can be prevented and it is obvious in case XI and case XII. In case XIII, due to the region of high turbulence intensity, the flow covers less space than the length of the wing chord, so the separated bubble slowly gets a chance to lengthen and returns to the surface later.

To better understand the fundamental of flow physics around tubercle wings while the maximum thickness location ratio changes, Fig. 22 compares the flow separation area's height of the three tubercle leading edge wings. The bubble height in case XIII is 15%c while this height in other cases such as case XI and case XII are about 10%c and 13%c, respectively. As a matter of the previous fact, this study concludes that by growing the maximum thickness location ratio from 0.26 c to 0.51 c, the height of the laminar separation bubble gradually rises around 5% of the mean chord.

To examine this conduct, an assessment is performed on the range of the lift coefficient, which is denoted by the power spectral density (PSD) against the frequency over time. The lift coefficient spectra for two distinct sinusoidal wings with dissimilar maximum thickness locations are depicted in figure 23 for comparison purposes.

More ever, we note from the overhead figure, the spectra of case XI (0.26 c) demonstrate much lower intensity, indicating that the fluctuations are weaker in this case compared to case XII (0.48 c). It can obviously perceived that the discretization utilized in these simulations has the ability to adequately capture flow scales deep into the inertial range, thus indicating its potential to deliver precise outcomes.

According to Fig. 23, there is a small peak at 1.36 Hz with some indication of a peak at very low frequencies with similar magnitude. In each of these forms, there is an initial peak that corresponds to the vortex fall. It is predicted that the second peak is related to the repetitive pressure drop in each of the vortices. This is while the main peak is related to the rotation by the velocity induced between two consecutive vortices with asymmetric rotation. It appears sensible that the vortices would follow the wake downwards and then affect both the lift and drag.

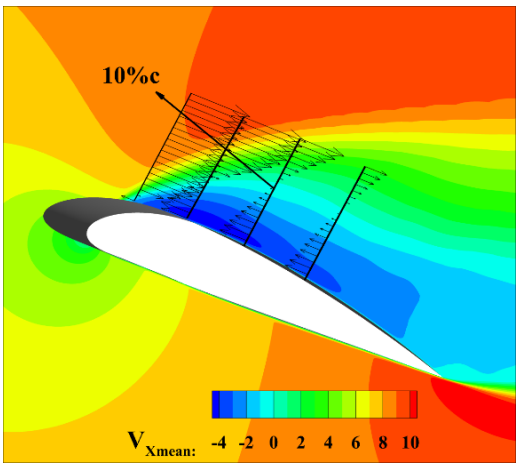

(a) Case XI (0.26 c)

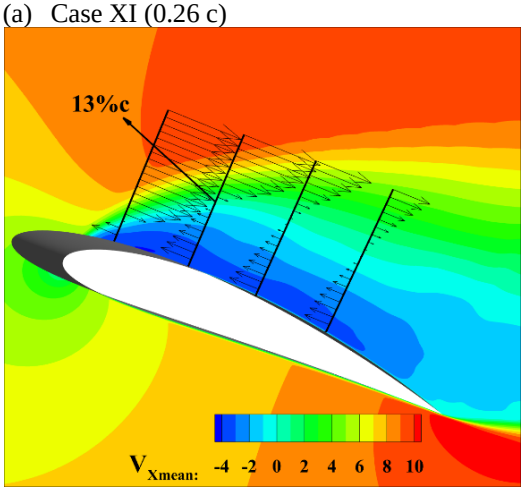

(b) Case XII (0.48 c)

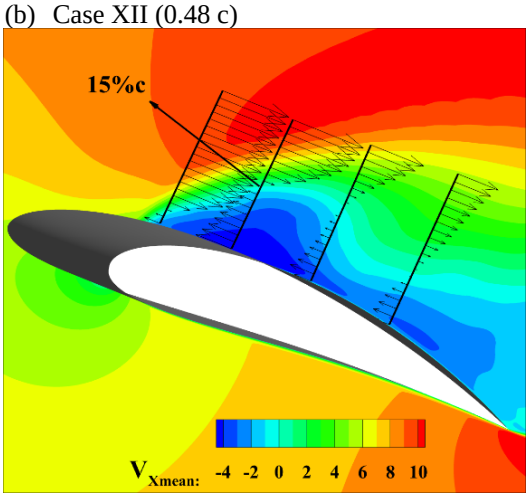

(c) Case XIII (0.51 c)

Fig. 22. Time-averaged streamwise velocity for three different sectional maximum thickness locations.

Also, it is conceivable the secondary peak is showing up in the lift due to slight bleeding of the drag force into the lift force due to slight inaccuracies.

As a conclusion of this section, it can be concluded that by increasing the location of maximum thickness from 0.26 c to 0.48 c the fluctuation goes up somehow because of the 3 deep fluctuations (1.36, 2.53, and 5.3 Hz) in case XII but the power spectral density in lift coefficient, in this case, is lower than case XI.

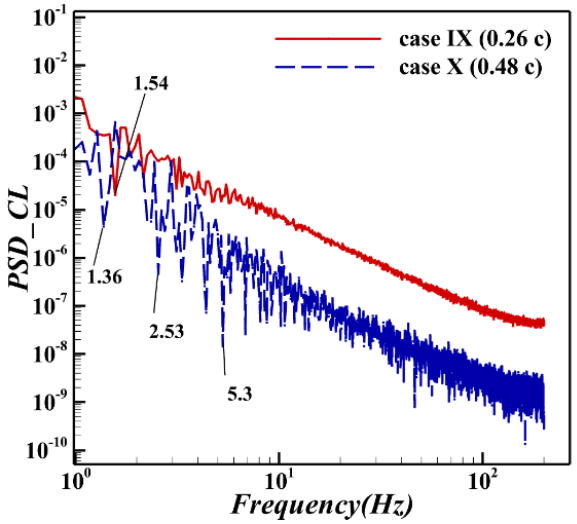

Fig. 23. Power spectral density of lift coefficient of tubercle leading edge wing with two different maximum thickness locations.

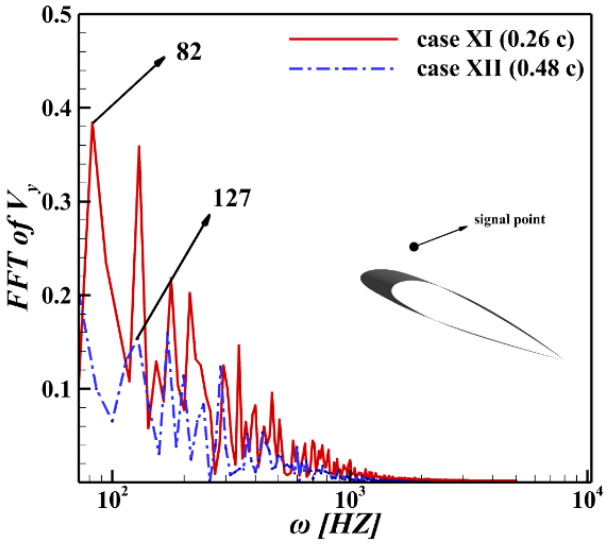

Fig. 24. Frequency response of the vertical velocity (y-velocity) in the flow around the tubercle infinite wings for three different maximum thickness locations.

To study the maximum thickness location's effect on the flow-induced vibrations, the vortex shedding frequency must be quantified initially. The dominant frequency of the fluid flow can portray the majority of the vortices' performance and structure on the infinite sinusoidal leading edge wing. Therefore, the frequency progress of the instantaneous vertical velocity component at the signal point is determined in Fig. 24 and the shedding frequency is found to be 82 Hz for case XI (0.26 c). It is worth mentioning that the resonant frequency related to case XII (0.48 c) is equal to 127 Hz. The time evolution of the instantaneous vertical velocity (Y-velocity) at a point close to the leading edge and on the upper surface of wing is mentioned for 12.51 seconds (5342 sampling data). Then, the time domain is changed to the frequency response by using Fast Fourier transformation and the shedding frequency is found.

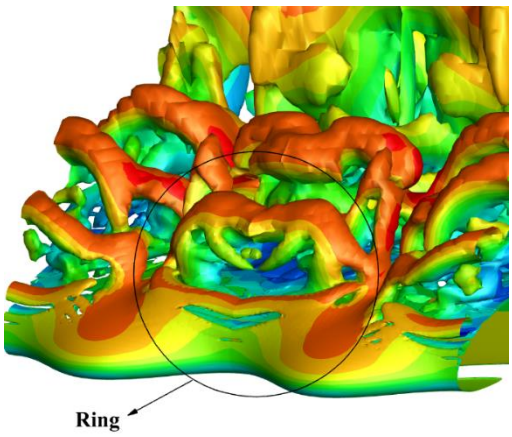

(a) Case XI (0.26 c)

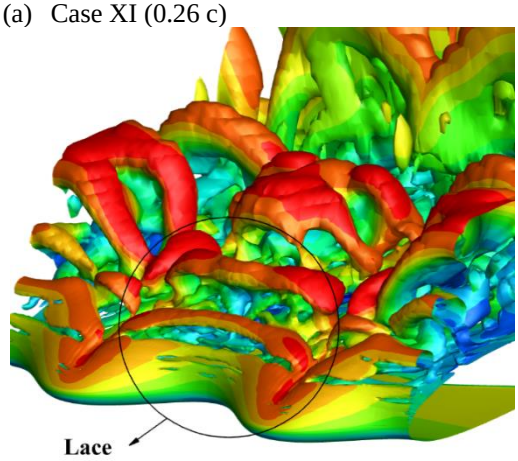

(b) Case XII (0.48 c)

Fig. 25. Q-criterion distribution between two different sectional maximum thickness locations colored by streamwise velocity.

Furthermore, the signal obtained from the numerical simulation is very clean without any physical noises; anyway, the Hanning window function is applied, although different windows do not change on the frequency domain. Furthermore, the selected point is in

the corridor of vortex shedding and the vertical velocity shows the fluctuation of a vortex; therefore, the dominant frequency can demonstrate the power of the vortex passing around the wing and the extracted results can be argued from the point of frequency view. In a nutshell, the frequency becomes larger by rising the sectional maximum thickness location.

Since protuberances on the leading edge of the wing generate a net downwash at the peaks' spanwise area, the maximum thickness location can change the structure of the vortex on the suction side of the infinite wing. It is probable that the primary contributors to this phenomenon are ring vortices originating from low-pressure areas located at troughs. Certainly, the unsteady individualities of the vortices can be imitated by the instantaneous flow field like Q-criterion displays in Fig. 25. In this illustration, the effect of maximum thickness locations are shown and the vortices are connected at the beginning of the formation when the maximum thickness location is closer to the leading edge. However, by moving this location backward of the airfoil, the flow can spread and a Lace-like structure is formed. In other words, the number of lumps in case XII is more than that of case XI due to the shear force enhancement.

5. CONCLUSION

In order to upsurge the maneuverability of MAVs, tubercle leading edge is a miscellaneous option. As the extracted information from previous studies of tubercle leading edge wings, the biggest benefit in using this type of flow control is that they have better aerodynamic performance than baseline wings in post stall condition. As mentioned before, not much attention has been paid to geometrical parameters in the post-stall circumstance, to understand better the performance of the flow distribution around the tubercle leading edge wings, this paper tries to examine the effect of the geometrical characteristics of TLE wing at post stall condition. The five design variables are considered to underestimate the best value to achieve maximum output. For this purpose, numerical simulation around the tubercle leading edge wing is performed at post-stall condition (22 degrees) and the DES turbulence model has been used to increase the accuracy of solving and simulating all types of eddies. Finally, the effect of each of these variables on the aerodynamic coefficients is investigated and the outcomes specify that:

- As reducing the amplitude ratio of the tubercle leading edge wing from 8.3%c to 5.8%c, the lift coefficient grows about 3.5%; otherwise, the drag coefficient reduces about 6%. The FSA's height reduces from 18%c to 13%c. However, the air dry zone shrinks by about $0.0064m^2$.

- With decreasing wavelength, the lift coefficient and drag coefficient go down, and also it would be visible for lift to drag ratio condenses by about 3.74%. On the other hand, the height of the flow separation area (FSA) decreases about 2.5% of the mean chord and the width of the FSA diminishes about 25% of the mean chord.

- As the sectional thickness ratio increases from 10.55%c to 18.14%c, the lift and drag coefficient decrease about 9.4% and 2.9%, respectively. Hence the FSA height and width reduce about 8.5%c and 2%c, respectively. Furthermore, the air dry zone growth from $0.005m^2$ to $0.0014m^2$.

- By raising the camber sectional ratio from 2.56%c to 3.34%c, drag coefficient lift increases and the FSA increases. Also, the air dry zone increases about $0.0248m^2$.

- As increasing the maximum thickness location ratio in the tubercle leading-edge wing, the L/D goes up by about 13.7%. Moreover, the height of the flow separation area (FSA) increases by about 5%c.

Furthermore, the tubercle leading edge wings has better performance than baseline wing in post stall nut the main problem of them are in pre stalls. Hence, the tubercle leading edge wings have less lift to drag ratio (L/D) than baseline wing and that's their limitations.

Furthermore, the following suggestion could be the main topic for upcoming research:

- ✓ Performing an optimization to solve the tubercle leading edge wings main problem in pre stall.
- ✓ Performing optimization to get the best geometrical parameters in post stall.

CONFLICT OF INTEREST

This is the original work of the authors and all authors have seen and approved the final version of the manuscript being submitted. The material described here is not under publication or consideration for publication elsewhere.

AUTHOR CONTRIBUTIONS

Mr. Amirfarhang Nikkhoo conducted the numerical simulation and analyzed the results; Dr. Ali Esmaeili planned the scheme, initiated the project, and suggested the simulation; also, Mr. Nikkhoo developed the simulation result and modeling and examined the theory validation. The manuscript was written through the contribution of all authors. All authors discussed the results, reviewed, and approved the final version of the manuscript.

REFERENCES

Barlow, J., Rae, W., & Pope, A. (1999). *Low-speed wind tunnel testing*.

Bolzon, M. D., Kelso, R. M., & Arjomandi, M. (2016). *Parametric study of the effects of a tubercle's geometry on wing performance through the use of the lifting-line theory*. 54th AIAA Aerospace Sciences Meeting, 0. https://doi.org/10.2514/6.2016-0295

Brodie, P. (1977). Form, function and energetics of Cetacea: a discussion. *Functional Anatomy of Marine Mammals*, 3, 45-58.

Canning, C., Crain, D., Eaton, T. S., Nuessly, K., Friedlaender, A., Hurst, T., Parks, S., Ware, C., Wiley, D., & Weinrich, M. (2011). Population-level lateralized feeding behaviour in North Atlantic humpback whales, Megaptera novaeangliae. *Animal Behaviour*, 82(4), 901–909. https://doi.org/10.1016/J.ANBEHAV.2011.07.031

Chaitanya, P., Joseph, P., Narayanan, S., Vanderwel, C., Turner, J., Kim, J. W., & Ganapathisubramani, B. (2017). Performance and mechanism of sinusoidal leading edge serrations for the reduction of turbulence-aerofoil interaction noise. *Journal of Fluid Mechanics*, 818, 435–464. https://doi.org/10.1017/jfm.2017.141

Coleman, H. W., & Steele, W. G. (2012). Engineering application of experimental uncertainty analysis. *AIAA Journal*, 33(10), 1888–1896. https://doi.org/10.2514/3.12742

Custodio, D., Henoch, C. W., & Johari, H. (2015). Aerodynamic characteristics of finite span wings with leading-edge protuberances. *AIAA Journal*, 53(7), 1878–1893. https://doi.org/10.2514/1.J053568

Delgado, H. E. C., Esmaeili, A., & Sousa, J. M. M. (2014). *Stereo PIV measurements of low-aspect-ratio low-reynolds-number wings with sinusoidal leading edges for improved computational modeling*. 52nd AIAA Aerospace Sciences Meeting - AIAA Science and Technology Forum and Exposition, SciTech 2014. https://doi.org/10.2514/6.2014-1280

Esmaeili, A. (2018). *Experimental and computational investigation of hybrid passive-active stall control for micro aerial vehicles*. Universiade De Lisboa Instituto Superior TÉcnico.

Esmaeili, A., Delgado, H. E. C., & Sousa, J. M. M. (2018). Numerical simulations of low-Reynolds-Number flow past finite wings with leading-Edge protuberances. *Journal of Aircraft*, 55(1), 226–238. https://doi.org/10.2514/1.C034591

Esmaeili, A., & Nikkhoo, A. (2021). Investigation of Thickness, Camber and Maximum Proximity Effect on Infinite Wavy Wing. *Journal of Aeronautical Engineering*, 23(1), 73–85. https://doi.org/10.22034/joae.2021.139477

Fish, F. E. (2020a). *Biomimetics and the Application of the Leading-Edge Tubercles of the Humpback Whale Flipper*. Flow Control Through Bio-inspired Leading-Edge Tubercles, Springer, Cham.

Fish, F. E. (2020b). *Biomimetics and the Application of the Leading-Edge Tubercles of the Humpback Whale Flipper*. Flow Control Through Bio-inspired Leading-Edge Tubercles, Springer, Cham.

Guerreiro, J. L. E., & Sousa, J. M. M. (2012). Low-reynolds-number effects in passive stall control using sinusoidal leading edges. *AIAA Journal*, 50(2), 461–469. https://doi.org/10.2514/1.J051235

Hansen, K. L., Kelso, R. M., & Dally, B. B. (2010). An investigation of three-dimensional effects on the performance of tubercles at low Reynolds numbers. *17th Australasian Fluid Mechanics Conference 2010*, 256–259.

Hansen, K. L., Kelso, R. M., & Dally, B. B. (2011). Performance variations of leading-edge tubercles for distinct airfoil profiles. *AIAA Journal*, 49(1), 185–194. https://doi.org/10.2514/1.J050631

Jabbari, H., Ali, E., & Djavareshkian, M. H. (2021a). Acoustic and phase portrait analysis of leading-edge roughness element on laminar separation bubbles at low Reynolds number flow: https://doi.org/10.1177/09544100211044316

Jabbari, H., Djavareshkian, M. H., & Esmaeili, A. (2021b). Static roughness element effects on protuberance full-span wing at micro aerial vehicle application: https://doi.org/10.1177/09544100211049932

Kelso, R., Rostamzadeh, N., & Hansen, K. (2020). *Tubercle geometric configurations: optimization and alternatives*. Flow Control Through Bio-inspired Leading-Edge Tubercles, Springer

International Publishing.

Langtry, R. B., Menter, F. R., Likki, S. R., Suzen, Y. B., Huang, P. G., & Völker, S. (2006). A correlation-based transition model using local variables - Part II: Test cases and industrial applications. *Journal of Turbomachinery*, 128(3), 423–434. https://doi.org/10.1115/1.2184353

Liang, Y., Yang, Y., Shan, X., & Wang, Z. (2022). Effect of Airfoil Dimple on Low-Reynolds-Number Differing Laminar Separation Behavior via Multi-Objective Optimization. *Journal of Aircraft*, 59(5). https://doi.org/10.2514/1.C036558

Madsen, C. J., & Herman, L. M. (1980*). Social and ecological correlates of vision and visual appearance*. Cetacean behavior: Mechanisms and Functions.

Miklosovic, D. S., Murray, M. M., & Howle, L. E. (2007). Experimental evaluation of sinusoidal leading edges. *Journal of Aircraft*, 44(4), 1404–1408. https://doi.org/10.2514/1.30303

Miklosovic, D. S., Murray, M. M., Howle, L. E., & Fish, F. E. (2004). Leading-edge tubercles delay stall on humpback whale (Megaptera novaeangliae) flippers. *Physics of Fluids*, 16(5). https://doi.org/10.1063/1.1688341

Mueller, T. J., & DeLaurier, J. D. (2003). Aerodynamics of small vehicles. *Annual Review of Fluid Mechanics*, *35*, 89–111. https://doi.org/10.1146/ANNUREV.FLUID.35.101101.161102

Nikkhoo, A., & Esmaeili, A. (2023). Effect of different aero-structural optimization in the commercial airplane. *Journal of Computational Applied Mechanics*, 54(2), 268-284 https://doi.org/10.22059/jcamech.2023.355499.809

Nili-Ahmadabadi, M., NematolahiI, O., & Kim, K. C. (2019). Effects of coarse riblets on air flow structures over a slender delta wing using particle image velocimetry. *Chinese Journal of Aeronautics*, 32(6), 1367–1379. https://doi.org/10.1016/j.cja.2019.03.019

Pereira, J. C. F., & Sousa, J. M. M. (1993). Finite Volume Calculations of Self-Sustained Oscillations in a Grooved Channel. *Journal of Computational Physics*, 106(1), 19–29. https://doi.org/10.1006/jcph.1993.1087

Rostamzadeh, N., Hansen, K., & Kelso, R. (2020). Tubercled Wing Flow Physics and Performance. *Flow Control Through Bio-Inspired Leading-Edge Tubercles*, 41–68. https://doi.org/10.1007/978-3-030-23792-9_2

Tomilin, G., A. (1957). Cetacea. *Mammals of the U.S.S.R. and Adjacent Countries*, 8(3), 155–165. https://doi.org/10.2517/PRPSJ.8.155

Winn, H. E. (1985). Humpback whale Megaptera novaeangliae (Borowski, 1781).In, Ridgway, SH and Harrison, RJ eds., Handbook of Marine Mammals. *The Sirenians and Baleen Whales*, 3, 241–273.